MITSUBISHI ELECTRIC RESEARCH LABORATORIES
https://www.merl.com

Model Parameter Identification for Induction Motor Fault Diagnosis

Benninger, Moritz; Wang, Bingnan; Inoue, Hiroshi

TR2026-122 September 09, 2026

Abstract

Modified Winding Function Theory (MWFT) offers a practical compromise between the simplicity of equivalentcircuit model and the high fidelity of finite-element analysis for induction motor fault analysis. However, the model requires a large number of geometric, electrical, magnetic, and mechanical parameters, many of which are unavailable for inservice machines. This paper presents a two-stage parameteridentification workflow for MWFT models when only nameplate data and a small set of benchmark measurements in healthy motor state are available. First, physically plausible initial values are derived from standard induction motor design rules. Second, the parameter set is refined by Differential Evolution to minimize the mismatch between simulated and expected current and speed. The method is evaluated on two squirrel-cage induction motors and then used to simulate rotor eccentricity as well as brokenbar faults. The results show that nameplate-based initialization already reproduces the characteristic fault frequencies, while measurement-assisted refinement improves agreement in both frequency location and amplitude. The proposed workflow makes MWFT-based fault modeling more practical for motors whose detailed design data are not available.

International Conference on Electrical Machines (ICEM) 2026

Mitsubishi Electric Research Laboratories, Inc.
201 Broadway, Cambridge, Massachusetts 02139

Model Parameter Identification for Induction Motor Fault Diagnosis

Moritz Benninger
Mitsubishi Electric Research Laboratories
201 Broadway, Cambridge, MA 02478
0000-0002-3485-4958

Bingnan Wang
Mitsubishi Electric Research Laboratories
201 Broadway, Cambridge, MA 02478
bwang@merl.com

Hiroshi Inoue
Advanced Technology R&D Center
Mitsubishi Electric Corporation
Amagasaki, Hyogo 661-8661 Japan

***Abstract*—Modified Winding Function Theory (MWFT) offers a practical compromise between the simplicity of equivalent-circuit model and the high fidelity of finite-element analysis for induction motor fault analysis. However, the model requires a large number of geometric, electrical, magnetic, and mechanical parameters, many of which are unavailable for in-service machines. This paper presents a two-stage parameter-identification workflow for MWFT models when only nameplate data and a small set of benchmark measurements in healthy motor state are available. First, physically plausible initial values are derived from standard induction motor design rules. Second, the parameter set is refined by Differential Evolution to minimize the mismatch between simulated and expected current and speed. The method is evaluated on two squirrel-cage induction motors and then used to simulate rotor eccentricity as well as broken-bar faults. The results show that nameplate-based initialization already reproduces the characteristic fault frequencies, while measurement-assisted refinement improves agreement in both frequency location and amplitude. The proposed workflow makes MWFT-based fault modeling more practical for motors whose detailed design data are not available.**

I. Introduction

Induction motors remain the workhorse of industrial drives, and their high reliability requirements make condition monitoring an essential part of maintenance strategies. Among the available signals, stator current is especially attractive because it is typically measured for control and protection and can be acquired without additional sensor installations. This has motivated extensive work on *motor current signature analysis* (MCSA), where fault-induced modulations are detected through spectral components and their evolution over time [1]–[3]. Although data-driven approaches have advanced rapidly in recent years [4], physics-guided interpretation remains valuable because it explains which spectral lines should appear for a given defect mechanism and operating point. Physics-based models are also an important building block for digital twins of rotating machines. Once parameterized, such a model can run alongside a deployed drive to estimate internal electromagnetic states that are not directly measurable and to predict how incipient faults evolve under changing load and speed conditions. This enables condition monitoring and predictive maintenance across diverse motor fleets without retraining a diagnostic model for every new asset.

In this paper, we focus on *modified winding function theory* (MWFT), a coupled-circuit framework that captures slotting effects and air-gap non-uniformity while remaining far less expensive than full finite-element analysis [5]–[7]. One main challenge is that MWFT requires a large set of motor-specific parameters, including geometric dimensions, winding layout, and electrical and magnetic constants. In practice, those parameters are rarely available with sufficient accuracy for in-service machines, especially across motors from different manufacturers. As a result, a naively parameterized MWFT model may reproduce qualitative trends while still missing the quantitative mapping between a physical defect and its expected MCSA signature.

To address this gap, we present a parameter-identification workflow that targets the realistic case in which only nameplate data and limited benchmark measurements are available. The main contributions of this paper are as follows:

- A two-stage identification workflow that combines analytical initialization from induction motor design rules with numerical optimization refinement by Differential Evolution.
- A parameter-specific search space design that uses engineering priors and sensitivity information to preserve physical plausibility while keeping the optimization tractable.
- An experimental evaluation on two squirrel-cage induction motors showing how the identified MWFT model can be used to simulate broken-bar and eccentricity faults.
- A practical discussion of when nameplate-only identification is sufficient and when additional measurements in healthy state are needed to improve frequency and amplitude agreement.

The remainder of the paper is organized as follows. Section II summarizes the MWFT model and the parameter set to be identified. Section III describes the proposed identification framework. Section IV presents the experimental evaluation and discusses the results. Section V concludes the paper.

II. MWFT Model and Parameter Set

In the MWFT model, the motor dynamics are represented by coupled stator and rotor circuit equations. For a three-phase squirrel-cage induction motor with N_p stator phases and N_r rotor bars, the electrical dynamics are written in vector-matrix form as

$$V_s = R_s I_s + \frac{d\Lambda_s}{dt} \tag{1}$$

$$\Lambda_s = L_{ss} I_s + L_{sr} I_r \tag{2}$$

$$V_r = R_r I_r + \frac{d\Lambda_r}{dt} \tag{3}$$

$$\Lambda_r = L_{rs} I_s + L_{rr} I_r \tag{4}$$

where $V_s = [V_{s1} V_{s2} \dots V_{sN_s}]$ and $V_r = [0]$ denote stator and rotor voltages, $I_s = [I_{s1} I_{s2} \dots I_{sN_p}]$ and $I_r = [I_{r1} I_{r2} \dots I_{rN_r}]$ denote stator and rotor currents, R_s and R_r are the resistance matrices, and Λ_s and Λ_r are the flux linkage matrices.

The electromagnetic torque and the mechanical dynamics are then given by

$$T_e = \frac{1}{2} I_s^\top \frac{\partial L_{ss}}{\partial \theta_r} I_s + I_s^\top \frac{\partial L_{sr}}{\partial \theta_r} I_r + \frac{1}{2} I_r^\top \frac{\partial L_{rr}}{\partial \theta_r} I_r \tag{5}$$

$$\frac{d\omega_r}{dt} = \frac{1}{J}(T_e - T_L - D_R \omega_r) \tag{6}$$

$$\frac{d\theta_r}{dt} = \omega_r \tag{7}$$

where θ_r is the mechanical rotor angle, ω_r is the mechanical angular speed, T_L is the load torque, D_R is the friction factor, and J is the rotor inertia.

The inductance terms in (2)-(4) and their derivatives in (5) are obtained from MWFT. The inductance between two windings is computed by integrating the product of the corresponding winding functions and the air-gap permeance over the stator circumference:

$$L_{ij}(t) = \frac{\mu_0 r l}{2\pi} \int_0^{2\pi} n_i(\phi, t)\, M_j(\phi, t)\, g^{-1}(\phi, t)\, d\phi \tag{8}$$

where μ_0 is the permeability of free space, r is the air-gap radius, l is the stack length, $n_i(\phi, t)$ is the turns-distribution function of winding i, $M_j(\phi, t)$ is the modified winding function of winding j, and $g(\phi, t)$ is the air-gap function. In practical induction motors, stator and rotor slotting effectively increase the air-gap length. This effect is captured through Carter's coefficient K_C, which represents the slotting-induced enlargement of the effective air-gap.

Different fault mechanisms enter the model through different physical pathways. In eccentricity faults, the air-gap function $g(\phi, t)$ must be modified to represent the nonuniform air-gap accurately [5], [8], [9]. In broken-bar faults, the rotor asymmetry is introduced through modified rotor resistance and inductance matrices [10], [11]. This direct mapping from physical defect to model structure is what makes MWFT attractive for fault simulation and diagnosis.

Applying MWFT to a specific machine requires parameters that span geometry, winding layout, electrical behavior, magnetic correction factors, and mechanical dynamics. Table I groups the model parameters considered in this work. Estimating these quantities from nameplate information of a machine and limited measurement data is the central identification problem addressed by the proposed method.

TABLE I

MWFT MODEL PARAMETERS TO BE IDENTIFIED (SCALARS)

Group	Parameter	Notation
Geometry	Air-gap radius	r
	Stack length	l
	Air-gap length	g
Winding layout	Number of stator turns	w
	Number of stator slots	N_s
	Number of rotor bars	N_r
Electrical	Stator resistance	R_s
	Stator leakage inductance	L_s
	Rotor bar resistance	R_b
	Rotor bar leakage inductance	L_b
	End ring resistance	R_e
	End ring leakage inductance	L_e
Magnetic correction	Saturation factor	k_{sat}
	Carter's coefficient	K_C
Mechanical	Inertia	J
	Friction factor	D_R

III. Parameter Identification Framework

A. Workflow overview

Reliable parameter identification requires at least a minimal set of machine information. In practice, the only universally available source is the nameplate of the machine, so we treat nameplate ratings as the baseline data set for initializing the MWFT model parameters. Standard induction motor design relations are first used to compute physically plausible starting values for the electrical circuit and mechanical parameters. When additional measurements in healthy motor state are available, the same initial model can be refined to match the specific machine more closely.

Figure 1 summarizes the proposed workflow. The first stage uses design rules to initialize the MWFT model from a minimal baseline data set. The second stage formulates parameter identification as a numerical optimization problem in which the remaining mismatch between simulation and reality is minimized by a derivative-free search. Once the parameters are identified, the calibrated model can be used to simulate both healthy operation and faulted cases such as broken rotor bars and eccentricity by applying the respective fault mechanism to the model.

B. Baseline data

The baseline data consist of the nameplate information and, optionally, additional measurements from one or more healthy operating states when available. Nameplate information is required because it supports the analytical initialization step. While the exact fields vary across regions and standards, most machines provide rated voltage V_n, current I_n, frequency f_n, speed ω_n, power P_n, pole-pair number p, efficiency η_n, and power factor PF_n. The rated torque T_n follows from the rated power and speed:

$$T_n = \frac{P_n}{\omega_n}. \tag{9}$$

For the numerical refinement stage, nameplate data can still be used, but additional measurements in healthy states

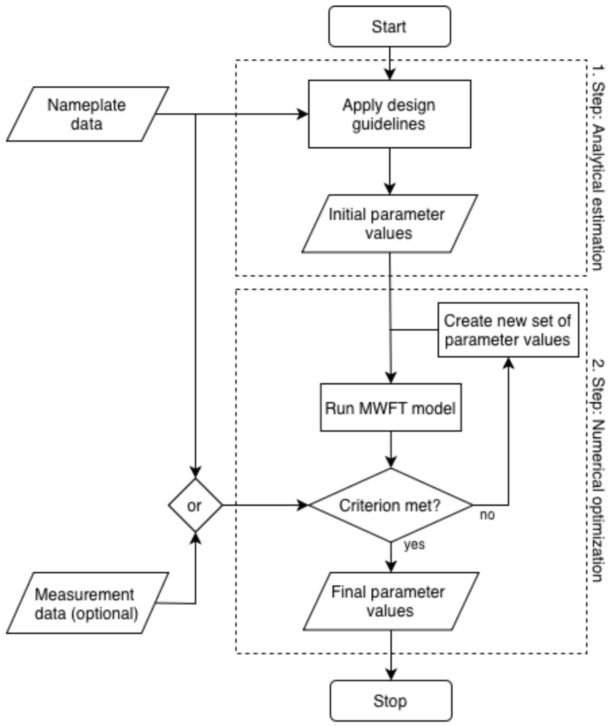

Fig. 1. Two-stage parameter-identification workflow. Analytical initialization produces physically plausible starting values, which are then refined numerically using nameplate data and, when available, measurement data.

strengthen the optimization considerably. Current measurements are especially informative because they capture the machine behavior most directly. In addition, voltage, speed, and torque measurements are needed so that the model inputs and outputs are fully specified for the chosen operating point.

C. Stage 1: analytical initialization

The goal of the analytical stage is not to recover the exact machine design, but to place the subsequent numerical optimizer in a physically meaningful region of the parameter space. We therefore use well-established induction motor design equations as engineering priors. These relations are particularly suitable because they are intended for the design stage, where only a limited number of high-level specifications are known.

Geometric dimensions: The overall size of the motor is estimated with the classical machine sizing equation

$$P_n = CD^2 l\omega_n \tag{10}$$

where C is the machine constant and D is the stator inner diameter [12]. To resolve (10) into air-gap radius r and stack length l, we use the ratio

$$\chi = \frac{D}{l} \approx \frac{\pi}{2p}\sqrt[3]{p} \tag{11}$$

which lies in a comparatively narrow range for standard induction machines [13].

TABLE II
CANDIDATE STATOR-SLOT AND ROTOR-BAR COMBINATIONS USED DURING IDENTIFICATION (ADAPTED FROM [14])

Pole pairs	$N_s = 36$	$N_s = 48$	$N_s = 54$
2	$N_r = 26, 28, 44$	$N_r = 38, 40, 56$	$N_r = 46$
4	$N_r = 26, 28, 44$	$N_r = 34, 38, 40, 56$	–
6	$N_r = 46, 48$	$N_r = 58, 60, 64, 68$	$N_r = 42, 66$

The air-gap length g is estimated from rated power and pole-pair number using the empirical rules in Ref. [12]:

$$g = 0.4 \cdot \sqrt[4]{\frac{P}{1000}}\,\mathrm{mm}, \qquad p = 1 \tag{12}$$

$$g = 0.25 \cdot \sqrt[4]{\frac{P}{1000}}\,\mathrm{mm}, \qquad p > 1 \tag{13}$$

with a minimum practical value of 0.2 mm for manufacturing and operational reasons [13].

Slot numbers and turns: The stator-slot number N_s and rotor-bar number N_r are constrained by standard machine-design rules. Stator-slot counts are multiples of the three phases and the pole-pair number, with typical values of 24, 36, 48, 54, 60, and 72 [14]. Rotor-bar counts must also avoid combinations that promote noise, vibration, or cogging. Table II lists the combinations considered in this work.

If suitable measurement data is accessible, the number of rotor bars N_R can also be calculated from the principal slot harmonics in the current spectrum using

$$f_{PSH} = (k \cdot N_r \cdot \frac{1-s}{p} + \upsilon) \cdot f_n \tag{14}$$

where s is the slip, k is any positive integer, and υ is the order of stator time harmonic. Subsequently, the number of stator slots N_s can be determined using the combinations in Table II.

The number of stator turns w is estimated from the air-gap flux Φ_δ [12]. The flux is approximated as

$$\Phi_\delta = B_m \tau_p l \tag{15}$$

where B_m is the average flux density and τ_p is the pole pitch. For induction motors, empirical values of $B_m = 0.5 \ldots 0.7$ are typical [13]. Assuming $\Phi_\delta \approx \Phi_h$, $E_h = U_1$ for machines above 30 kW and $E_h = 0.95U_1$ for machines below 30 kW, and using a winding factor ξ of 0.96 for single-layer winding or 0.92 for twisted double-layer winding, the initial number of stator turns is estimated as the closest integer by

$$w = \frac{\omega}{\sqrt{2}}\,\xi\,\frac{\Phi_h}{E_h}. \tag{16}$$

Using the geometric dimensions and the stator and rotor slot numbers and turns, the complex winding distribution for machines with integral-slot windings can be calculated according to equation 8. In the case of fractional-slot windings, this approach is not feasible.

Resistive parameters: The stator resistance is estimated from the motor losses. Total losses P_{loss} are obtained from the efficiency η:

$$P_{\text{loss}} = \frac{P_n}{\eta} - P_n \tag{17}$$

The stator losses $P_{\text{loss},s}$ are calculated by the stator-loss share reported in [15]. The resulting stator resistance R_s is

$$R_s = \frac{P_{\text{loss},s}}{3I_n^2}. \tag{18}$$

Rotor-bar and end-ring resistances are estimated from the rotor-loss share together with the currents in the rotor bars and end rings. Using the stator current I_1, power factor $\cos\varphi$, and the phase numbers m and winding numbers w in stator and rotor, the rotor current is approximated by

$$I_2 = \frac{m_1 w_1}{m_2 w_2} I_1 \cos\varphi \tag{19}$$

which gives the cage-bar current

$$I_b = \frac{I_2}{p} \tag{20}$$

and the end-ring current

$$I_e = \frac{I_2}{2p\sin\left(\frac{\pi p}{N_R}\right)}. \tag{21}$$

The total rotor loss is then expressed as

$$P_{\text{loss},R} = N_R R_b I_b^2 + 2R_e I_e^2. \tag{22}$$

To separate R_b and R_e, we use approximate cross-sectional areas inferred from permissible current density:

$$A_b = \frac{I_b}{S_b}, \qquad A_e = \frac{I_e}{S_e} \tag{23}$$

and the resulting resistance ratio

$$R_b \approx \frac{\rho l}{A_b}, \qquad R_e \approx \frac{\rho(2\pi r)}{A_e}, \qquad \frac{R_e}{R_b} \approx \frac{(2\pi r) I_b}{l I_e}. \tag{24}$$

Given (22) and (24), either R_b or R_e can be solved first and the other obtained subsequently.

Leakage, saturation, and mechanical parameters: The stator leakage inductance is initialized from the rated impedance using the empirical approximation [16]

$$L_s = (0.1 \ldots 0.15) Z_n = (0.1 \ldots 0.15) \frac{U_n}{I_n}. \tag{25}$$

A fixed percentage of 12.5 % is used for getting a fixed parameter value.

The rotor-bar and end-ring leakage inductances follow from geometry-dependent stray-conductivity factors [12]:

$$L_b = \mu_0 l \lambda_{nz} \tag{26}$$

$$L_e = \mu_0 \frac{2\pi r}{N_R} \lambda_r. \tag{27}$$

For the values used here, $\lambda_{nz} = 0.66$ for the rotor bar and $\lambda_r = 0.25 \ldots 0.5$ for the end ring [12].

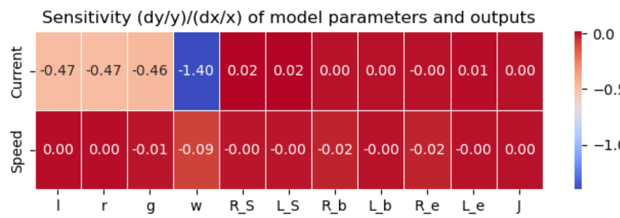

Fig. 2. Finite-difference sensitivity of speed and current with respect to model parameters, used to guide the parameter search-space design.

The friction factor is initialized from the mechanical-loss share reported in [15]:

$$D_R = \frac{P_{\text{loss,mech}}}{\omega_n}. \tag{28}$$

The inertia J is estimated from catalogue data for motors with similar power rating, pole-pair number, and efficiency class.

Because the internal magnetic conditions are unknown, the saturation factor k_{sat} is treated as an uncertain correction factor to the inductance values rather than estimated directly. Based on values used in prior MWFT studies, its admissible range is set to $0.6 \ldots 0.8$ [9]. For the same reason, Carter's coefficient is initialized with a wider uncertainty range and constrained to $K_C = 1.2 \ldots 1.6$ [9].

More detailed information on the design rules can be found in [12]–[14], [16].

D. Stage 2: numerical refinement

The analytical estimates are usually not accurate enough to model the target motor with sufficient fidelity. They therefore serve as starting values for a numerical refinement step. We use *Differential Evolution* because the identification problem is nonlinear, includes discrete and continuous parameters, and does not provide derivatives conveniently [11]. A population of candidate solutions is evolved over N iterations to minimize a fitness function. The main hyperparameters are the differential weight F, crossover probability CR, and population size NP.

1) Search-space design: A useful search space must satisfy two competing requirements: it should be broad enough to correct inaccuracies in the analytical initialization, but narrow enough to preserve physical plausibility and avoid unnecessary optimization effort. We therefore define the search space parameter by parameter, based on two criteria: the confidence in the analytical estimate and the sensitivity of the model outputs to that parameter.

To illustrate this rationale, a sensitivity analysis is performed for the 0.75 kW motor from Section IV. Each parameter is perturbed within $\pm 50\%$, and the resulting effect on the output current and speed is summarized in Figure 2.

The analysis shows that the air-gap radius r, stack length l, air-gap length g, and stator turns w strongly influence the outputs. Because these parameters also come from comparatively reliable design relations, their search ranges are kept tight at $\pm 10\%$. Stator resistance R_s, rotor-bar resistance R_b, end-ring resistance R_e, and stator leakage inductance L_s have

TABLE III
SEARCH SPACE FOR DIFFERENTIAL EVOLUTION

Parameter	Lower limit	Upper limit
Air-gap radius r	90 %	110 %
Stack length l	90 %	110 %
Air-gap length g	90 %	110 %
Number of stator turns w	90 %	110 %
Number of stator slots N_s	see Table II	see Table II
Number of rotor bars N_r	see Table II	see Table II
Stator resistance R_s	50 %	150 %
Stator leakage inductance L_s	50 %	150 %
Rotor bar resistance R_b	50 %	150 %
Rotor bar leakage inductance L_b	-	-
End-ring resistance R_e	50 %	150 %
End-ring leakage inductance L_e	-	-
Saturation factor k_{sat}	0.6	0.8
Carter's coefficient K_C	1.2	1.6
Inertia J	-	-
Friction factor D_R	90 %	110 %

lower output sensitivity and rely on additional assumptions during initialization; these are therefore allowed to vary more broadly, from 50% to 150% of their initial values. Rotor leakage inductances L_b and L_e, as well as inertia J, show negligible sensitivity in this study and are kept fixed. The friction factor D_R is weakly constrained by the data but is initialized from an established loss relation, so its search range is limited to $\pm 10\%$. The sensitivity analysis is used only as a guideline. The bounds are not derived directly from it, but are rather defined for general application. Table III summarizes the resulting bounds of the parameter search space for the Differential Evolution optimizer.

2) Fitness function: The fitness function measures the mismatch between simulation and reference data. Differential Evolution minimizes this quantity until the stopping criterion is met. When only nameplate data are available, the rated voltage U_n and torque T_n define the model input, while the rated current I_n and rated speed ω_n define the target output. In this case, the RMS current and mean speed are compared through

$$f = \frac{I_{\text{sim}} - I_{\text{real}}}{I_{\text{real}}} + \frac{\omega_{\text{sim}} - \omega_{\text{real}}}{\omega_{\text{real}}}. \tag{29}$$

When measurement data are available, the same structure is used, but the measured operating-point data replace the nameplate targets. If the current measurement has sufficient frequency resolution, the objective can also be defined in the frequency domain by comparing the n dominant spectral peaks:

$$f = \frac{1}{n} \sum_{i=1}^{n} \frac{I_{\text{sim},i} - I_{\text{meas},i}}{I_{\text{meas},i}} + \frac{\omega_{\text{sim}} - \omega_{\text{real}}}{\omega_{\text{real}}}. \tag{30}$$

This formulation allows the optimization to emphasize the spectral components that are most relevant for fault diagnosis.

TABLE IV
NAMEPLATE DATA OF THE TWO INDUCTION MOTORS USED FOR EVALUATION

Parameter	Motor 1	Motor 2	Unit
P_n	0.75	1.1	kW
f_n	60	50	Hz
U_n	200	400	V
I_n	3.3	2.5	A
n_n	1710	1445	1/min
PF_n	0.76	0.75	–
η_n	86.0	84.4	%
Connection	Delta	Star	–

IV. EXPERIMENTAL EVALUATIONS

A. Test motors and evaluation setup

The proposed workflow is evaluated on two squirrel-cage induction motors: a 0.75 kW motor and a 1.1 kW motor. Table IV summarizes their nameplate data. For the 1.1 kW motor, measurements are available for healthy operation, broken-rotor-bar operation, and mixed eccentricity under a nominal load of 7.27 Nm. For the 0.75 kW motor, measurements are available for healthy operation at 3.2 Nm and for static eccentricity at 3.5 Nm. This data set allows both execution of the proposed parameter identification workflow and validation against measured fault signatures.

For both motors, the parameters are identified twice: once using only nameplate data in the fitness function and once using measurement data. In the latter case, the measurement data is used to identify the stator slots and rotor bars via the principal slot harmonics before optimization ($N_s = 36$ and $N_r = 28$). The Differential Evolution hyperparameters $F = 0.95$, $CR = 0.7$, $NP = 10$, $N = 10$ were adopted from [11] due to their good convergence behavior. The optimization is terminated when the fitness reaches $f < 0.01$. The optimizer needs an average of 65.6 iterations ($\sigma = 33.9$) to converge over 10 runs when using nameplate data and an average of 73.6 iterations ($\sigma = 34.5$) when using measurement data. With a computational time of approximately 5 seconds per simulation, the optimization process takes between 1 and 7 minutes.

B. Fault simulation results

The identified parameter sets are then used to simulate the relevant fault conditions. Figures 3 and 4 compare the simulated and measured current spectra.

1) Identification from nameplate data: For the 0.75 kW motor with static eccentricity, the parameter set identified from nameplate data reproduces the expected fault components well, but the simulated sideband frequencies differ slightly from the measurements: the measured components appear at 31 Hz and 89 Hz, while the simulation predicts 32 Hz and 88 Hz. This discrepancy is consistent with a small error in the modeled operating speed. The amplitude deviation is approximately 2 dB. For the 1.1 kW motor with a broken rotor bar, the identified model reproduces the frequency location of the characteristic sideband harmonics. However, the amplitude

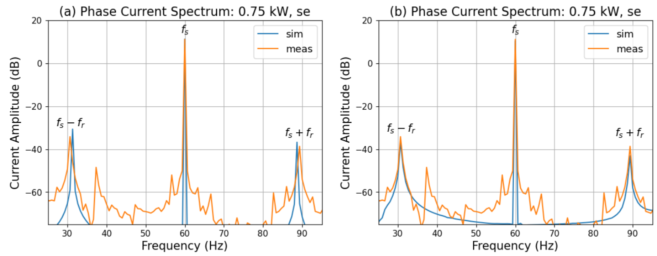

Fig. 3. Static-eccentricity spectra for the 0.75 kW motor. (a) Parameters identified from nameplate data only. (b) Parameters identified using measurement data.

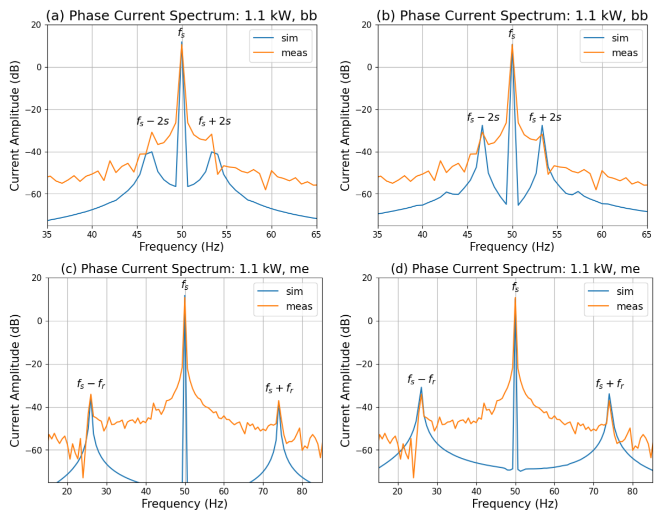

Fig. 4. Measured and simulated spectra for the 1.1 kW motor. (a)–(b) Broken-bar (BB) case with parameters identified from nameplate data and measurement data, respectively. (c)–(d) Mixed-eccentricity (ME) case with parameters identified from nameplate data and measurement data, respectively.

agreement is limited when the parameters are identified from nameplate data alone because the number of rotor bars is not identified correctly.

2) Identification from measurement data: When measurement data are included in the identification step for the 0.75 kW motor with static eccentricity, the actual operating speed is captured more accurately, and the simulated and measured fault frequencies and amplitudes align much more closely. For the 1.1 kW motor with a broken rotor bar, when measurement data are used during identification, the amplitude agreement improves to within approximately ± 3 dB. For mixed eccentricity, the measured spectral components are reproduced with an amplitude deviation of about ± 4 dB.

C. Discussions

Across both motors, two patterns stand out. First, nameplate-based initialization is already strong enough to reproduce the main diagnostic frequencies, which is important for practical deployment because nameplate data are almost always available. Second, the remaining mismatch is strongly influenced by quantities that are difficult to infer reliably from nameplate data alone, especially the actual operating speed and discrete structural parameters such as the rotor-bar count. Additional measurements therefore play a complementary role: they do not replace the analytical initialization, but they improve the model where nameplate-only identification remains ambiguous.

On the other hand, the comparison highlights an important fact that the identified parameters are not necessarily unique. Multiple parameter sets can produce similar outputs, especially when only nameplate data are available. While we demonstrated that with measured current data utilized in the identification process, the model can be improved and more closely align with the experiment measurements, additional measurements at multiple load and speed conditions will further address the identifiability challenge.

V. Conclusions

This paper presented a practical workflow for identifying MWFT parameters when detailed motor design data are unavailable. The method combines analytical initialization from standard induction motor design relations with a constrained Differential Evolution refinement step. Applied to two squirrel-cage induction motors, the resulting models reproduced the characteristic fault frequencies for broken-bar and eccentricity cases and showed improved spectral agreement when measurement data were included during identification. The workflow tackles the issue of non-uniqueness of the parameter sets by combining engineering priors with parameter-specific search bounds. The practical impacts of residual non-uniqueness are minimal, since the identified parameter sets found in this study model the induction motor with sufficient accuracy in both healthy and faulty states and are therefore interchangeable. However, identifiability remains a central challenge for applying MWFT models to motor condition monitoring and predictive maintenance. Future work will therefore focus on strengthening the objective with multi-operating-point measurements and on improving the treatment of discrete structural parameters such as rotor-bar count.

References

[1] M. E. H. Benbouzid, “A review of induction motors signature analysis as a medium for faults detection,” *IEEE transactions on industrial electronics*, vol. 47, no. 5, pp. 984–993, 2000.

[2] S. Nandi, H. A. Toliyat, and X. Li, “Condition monitoring and fault diagnosis of electrical motors – a review,” *IEEE transactions on energy conversion*, vol. 20, no. 4, pp. 719–729, 2005.

[3] W. T. Thomson and I. Culbert, *Current signature analysis for condition monitoring of cage induction motors: Industrial application and case histories*. John Wiley & Sons, 2017.

[4] S. Zhang, S. Zhang, B. Wang, and T. G. Habetler, “Deep learning algorithms for bearing fault diagnostics – a comprehensive review,” *IEEE Access*, vol. 8, pp. 29857–29881, 2020.

[5] H. A. Toliyat, M. S. Arefeen, and A. G. Parlos, “A method for dynamic simulation of air-gap eccentricity in induction machines,” *IEEE transactions on industry applications*, vol. 32, no. 4, pp. 910–918, 1996.

[6] G. Bossio, C. De Angelo, J. Solsona, G. O. Garca, and M. I. Valla, “Application of an additional excitation in inverter-fed induction motors for air-gap eccentricity diagnosis,” *IEEE Transactions on Energy Conversion*, vol. 21, no. 4, pp. 839–847, 2006.

[7] X. Li, Q. Wu, and S. Nandi, “Performance analysis of a three-phase induction machine with inclined static eccentricity,” *IEEE Transactions on Industry Applications*, vol. 43, no. 2, pp. 531–541, 2007.

[8] L. Zhou, B. Wang, C. Lin, H. Inoue, and M. Miyoshi, "Static eccentricity fault detection for psh-type induction motors considering high-order air gap permeance harmonics," in *2021 IEEE International Electric Machines Drives Conference (IEMDC)*, pp. 1–7, 2021.
[9] B. Wang, M. W. Albader, H. Inoue, and M. Kanemaru, "Induction motor eccentricity fault analysis and quantification with modified winding function based model," in *2022 25th International Conference on Electrical Machines and Systems (ICEMS)*, pp. 1–6, 2022.
[10] J. Tang, J. Chen, K. Dong, Y. Yang, H. Lv, and Z. Liu, "Modeling and evaluation of stator and rotor faults for induction motors," *Energies*, 2020.
[11] M. Benninger, M. Liebschner, and C. Kreischer, "Fault detection of induction motors with combined modeling- and machine-learning-based framework," *Energies*, vol. 16, no. 8, 2023.
[12] G. Müller, K. Vogt, and B. Ponick, *Berechnung elektrischer Maschinen*. Wiley, 2008.
[13] J. Pyrhönen, T. Jokinen, and V. Hrabovcov, *Design of rotating electrical machines*. Wiley, 2013.
[14] T. A. Lipo, *Introduction to AC machine design*. Wiley, 2017.
[15] L. Aarniovuori, M. Niemelä, J. Pyrhönen, W. Cao, and E. B. Agamloh, "Loss components and performance of modern induction motors," *2018 XIII International Conference on Electrical Machines (ICEM)*, 2018.
[16] A. Binder, *Elektrische Maschinen und Antriebe*. Springer Vieweg, 2017.

BIOGRAPHIES

M. Benninger was born in Germany. He received the B. Eng. in energy and environmental engineering from University of applied Sciences Ravensburg-Weingarten, the M. Sc. in systems engineering from University of applied Sciences Aalen and the Ph.D. degree in electrical engineering from Helmut-Schmidt-University, Hamburg in 2024. His current research focuses on electric machine analysis, modeling and fault diagnosis.

Bingnan Wang received his B.S. from Fudan University in 2003 and his Ph.D. from Iowa State University in 2009, both in Physics. He has been with Mitsubishi Electric Research Laboratories (MERL) since 2009, and is now a Senior Principal Research Scientist. His current research focuses on electric machine analysis, design optimization, fault diagnosis using both physics-based modeling and machine learning techniques.

Hiroshi Inoue received B.E.and M.E. degree from The University of Tokyo, Japan, in 2012 and 2014, respectively. He has been a researcher at Mitsubishi Electric Corporation since April 2014. His primary research focus is motor malfunction diagnosis technology. He is currently a member of the Mitsubishi Electric Advanced Technology R&D Center, Electromechanical Systems Department.